Science Advances AAAS

Manuscript Template

FRONT MATTER

Title

- Experimental Observation of Roton-Like Dispersion Relations in Metamaterials.
- Experimental Observation of Roton-Like Dispersion.

Authors

Julio Andrés Iglesias Martínez[1]†, Michael Fidelis Groß[2]†, Yi Chen[2]†*, Tobias Frenzel[2], Vincent Laude[1], Muamer Kadic[1,3], and Martin Wegener[2,3]*

Affiliations

[1]Institut FEMTO-ST, UMR 6174, CNRS, Université de Bourgogne Franche-Comté; Besançon 25030, France.

[2]Institute of Applied Physics, Karlsruhe Institute of Technology (KIT); Karlsruhe 76128, Germany.

[3]Institute of Nanotechnology, Karlsruhe Institute of Technology (KIT); Karlsruhe 76128, Germany.

*Correspondence to: yi.chen@partner.kit.edu (Y.C.); martin.wegener@kit.edu (M.W.)

† These authors contributed equally to this work.

Abstract

Previously, rotons were observed in correlated quantum systems at low temperatures, including superfluid helium and Bose-Einstein condensates. Here, following a recent theoretical proposal, we report the direct experimental observation of roton-like dispersion relations in two different three-dimensional metamaterials under ambient conditions. One experiment uses transverse elastic waves in microscale metamaterials at ultrasound frequencies. The other experiment uses longitudinal air-pressure waves in macroscopic channel-based metamaterials at audible frequencies. In both experiments, we identify the roton-like minimum in the dispersion relation that is associated to a triplet of waves at a given frequency. Our work shows that designed interactions in metamaterials beyond the nearest neighbors open unprecedented experimental opportunities to tailor the lowest dispersion branch – while most previous metamaterial studies have concentrated on shaping higher dispersion branches.

Teaser

Artificial materials support elastic or acoustic waves whose travel direction continuously changes from backward to forward.

MAIN TEXT

Introduction

In 1962, the Nobel Prize in Physics was awarded to Lev Landau "for his pioneering theories for condensed matter, especially liquid helium." Among other achievements, he suggested an unusual kind of dispersion relation for acoustical waves in superfluid ^{4}He at low temperatures, commonly referred to as the roton (*1*). Based on his (*1*) and Richard Feynman's (*2*, *3*) subsequent work, rotons were observed in inelastic neutron scattering experiments in 1961 (*4*). In brief, for the roton dispersion relation, energy and momentum of the wave are proportional to each other for small momenta. For larger momenta, a roton minimum of energy versus momentum occurs (*5*). Detailed theoretical (*6–10*) and experimental (*11–13*) investigations of this highly unusual dispersion relation in liquid ^{4}He remain subject of research until today (*14*). Rotons and roton-like dispersion relations, respectively, have also been investigated experimentally in other correlated quantum systems at low temperatures, such as quasi-two-dimensional thin films of ^{3}He (*15*), phonons along the (111) direction in solid helium (*16*), quantum Hall effect stripes in semiconductors (1*7–19*), and Bose-Einstein condensates of atoms (*20–25*).

In 2020 (*26*) and 2021 (*27*, *28*), respectively, two papers showed by theoretical calculations that roton-like dispersion relations may also occur in designed crystals or periodic metamaterials (*29*, *30*). Here, quantum effects and correlations would play no role and low temperatures, which often hinder applications, would not be needed. The first paper (*26*) builds on micropolar continuum elasticity theory (*31–33*). In this context, chirality based on broken centrosymmetry is a necessary condition for coupling to micro-rotations and hence for obtaining rotons (*26*). The second paper (*27*) suggests achiral and chiral three-dimensional periodic micro- and macrostructures. Herein, the mechanism for rotons is based on tailored third-nearest-neighbor interactions in addition to the usual nearest-neighbor interactions. For pronounced roton behavior, the effective strengths of the two interactions must be comparable.

In this paper, we follow the specific achiral structure blueprints of the second approach (*27*) and manufacture corresponding three-dimensional (3D) polymer-based metamaterials by 3D additive manufacturing. For each unit cell, we measure the nanometric displacement vectors for the 3D polymer-based microstructures, and the scalar air pressure modulation for the macroscopic airborne-sound samples, respectively. The unusual acoustical-phonon dispersion relations obtained by Fourier transformation agree well with calculated roton band structures as well as with numerical finite-element calculations for the finite-size samples. We show that the roton minimum is captured qualitatively by a generalized wave equation from an analytical higher-order-gradient effective-medium theory.

More broadly speaking, throughout the last two decades, a large number of scientific studies has worked on shaping wave propagation in metamaterials for higher phonon bands, including phononic band gaps, stop bands, topological band gaps, local resonances, Dirac points, Weyl points, etc. Strangely, our ability to shape wave propagation for the lowest phonon band has fallen behind. Tailoring interactions beyond the nearest neighbors opens a systematic route towards obtaining a large variety of behaviors for the lowest band. Here, we show that these possibilities are accessible experimentally and can be tailored towards wanted frequency ranges. Roton-like dispersion relations serve as an early example.

Results

Metamaterial Blueprints and Effective-Medium Description

The blueprints for the two achiral three-dimensional tetragonal-symmetry metamaterial structures suggested theoretically in Ref. (*27*) and investigated experimentally in this Article are illustrated in Fig. 1. For the elastic structure shown in Fig. 1(a), transverse-like as well as longitudinal-like waves propagate in the constituent elastic material and not in the voids within. Only the transverse-like waves will show the roton behavior. For the structure in Fig. 1(b), only longitudinal airborne pressure waves propagate in the voids within the material, and the material itself ideally merely provides rigid (Neumann) boundaries to the air flow in the channel system. In other words, Fig. 1(b) is roughly the geometrical complement of Fig. 1(a). In this work, we have made minor readjustments with respect to perfect complementarity to ease the manufacturing. The waves in the structure in Fig. 1(b) are closer to rotons in superfluid helium than the ones in Fig. 1(a) in the sense that both are longitudinal waves. Both architectures can be scaled to different absolute lattice constants $a_{xy} = 2a_z$. We choose to realize the architecture in Fig. 1(a) in microscopic form with $a_z = 100$ μm and that in Fig. 1(b) in macroscopic form with $a_z =$ 5 cm. Correspondingly, the two architectures operate in rather different frequency ranges: (a) at ultrasound and (b) at audible frequencies. Both metamaterial-beam samples considered have $N_z = 50$ metamaterial unit cells along the propagation direction (z-axis) and a finite cross section of (a) $N_x \times N_y = 2 \times 2$ and (b) $N_x \times N_y = 1 \times 1$ unit cells in the perpendicular xy-plane, respectively.

The mechanism leading to roton dispersion relations is the same for both metamaterials (*27*). The small cubic volumes (light yellow) act as "atoms", i.e., as masses and small gas reservoirs, respectively. The short (blue) cylindrical rods and channels, respectively, mediate the nearest-neighbor interaction ($N = 1$) between the atoms. All other beams and channels (red), respectively, serve to mediate the third-nearest-neighbor interaction ($N =$ 3). Intuitively, the length and cross section of the cylindrical elements effectively determine the strength of the corresponding interaction.

In Ref. (*27*), we have argued that the interplay of $N = 1$ and $N = 3$ contributions leads to a phonon mode hybridization and thereby to extraordinary Bragg reflections that give rise to the occurrence of the roton minimum within the first Brillouin zone of the metamaterial crystal. Interestingly, while this statement is valid, it is not necessary to invoke Bragg reflections to understand or reproduce the roton minimum. To appreciate this point, we make the transition to an effective-medium description. As usual, the effects of Bragg reflections do not occur in effective-medium continuum theory, for which one considers the limit $a_z \rightarrow 0$. For simplicity and corresponding to our experiments, we consider only waves propagating along the z-direction with wavenumber k_z for both, airborne pressure waves with the air-pressure modulation $\tilde{P}$, and elastic waves with the transverse displacement u. The wave amplitude, A, shall stand for either $\tilde{P}$ or u. For an infinitely extended periodic lattice, we have the equation of motion for the amplitude $A_n = A_n(t)$ at the integer lattice sites $n = z/a_z$ along the z-direction

$$\frac{\mathrm{d}^2 A_n}{\mathrm{d}t^2} = C_1\left(A_{n+1} - 2A_n + A_{n-1}\right) + C_3\left(A_{n+3} - 2A_n + A_{n-3}\right), \tag{1}$$

with the nearest-neighbor coupling coefficient $C_1 > 0$ and the third-nearest-neighbor coupling coefficient $C_3 \geq 0$ (cf. Supplementary Text). In the continuum limit, this equation of motion turns into the following generalized wave equation for the amplitude field $A = A(z,t)$

$$\frac{\partial^2 A}{\partial t^2} = c_2 \frac{\partial^2 A}{\partial z^2} + c_4 \frac{\partial^4 A}{\partial z^4} + c_6 \frac{\partial^6 A}{\partial z^6}, \tag{2}$$

with the three coefficients $c_2 = C_1 a_z^2 + 9C_3 a_z^2 > 0$, $c_4 = 6C_3 a_z^4 \geq 0$, and $c_6 = C_3 a_z^6 \geq 0$. The first two terms form an ordinary wave equation, whereas the fourth-order and sixth-order spatial derivatives with respect to z on the right-hand side, which are proportional to C_3, specifically originate from the third-nearest-neighbor interactions. Using a plane-wave ansatz $A(z,t) = B\cos(k_z z - \omega t)$, with constant prefactor B, we obtain the dispersion relation for the wave's angular frequency ω versus wavenumber k_z

$$\omega(k_z) = \omega(-k_z) = \sqrt{c_2 k_z^2 - c_4 k_z^4 + c_6 k_z^6}. \tag{3}$$

For the above coefficients c_2, c_4, and c_6, the root on the right-hand side does not become negative and, hence, the angular frequency ω is real valued. For small k_z, the dispersion relation approximately starts as $\omega(k_z) = \sqrt{c_2}\, k_z$, with phase velocity $\sqrt{c_2}$. For sufficiently large ratio C_3/C_1, with increasing k_z, $\omega(k_z)$ exhibits a maximum due to the negative fourth-order term, followed by the roton minimum due to the positive sixth-order term at yet larger k_z. Below, we will plot this approximate analytical effective-medium roton dispersion relation together with the more complete numerically calculated and the measured roton dispersion relations. In addition to the region of negative slope, $\mathrm{d}\omega/\mathrm{d}k_z < 0$, which results in backward waves, it contains an angular-frequency region in which one gets three solutions for the wavenumber k_z at a given angular frequency ω. Clearly, in the limit of $k_z \to \pi/a_z$, the higher-order-gradient effective-medium roton dispersion relation has the wrong asymptotics as it does not include the effects of Bragg reflections.

The Two Experiments

The microscale-sample experiments have been performed at Karlsruhe, the macroscale-sample experiments at Besancon. While many details are different, conceptually, the two experiments are closely similar: We launch a wave at one end of the finite-length metamaterial beam by a monochromatic excitation source, the frequency $f = \omega/(2\pi)$ of which is varied in small frequency steps Δf. We detect the resulting wave amplitude $A_n(t)$ versus real time t in each of the $n = 1, 2, \ldots, N_z = 50$ metamaterial unit cells at each frequency. We extract the complex-valued Fourier components, $\tilde{A}_n(\omega)$, at frequency ω. At each frequency, we normalize the data to unity power density, i.e., $\sum_{n=1}^{50} \left|\tilde{A}_n(\omega)\right|^2 = 1$. In this manner, we eliminate the frequency response of the excitation process. Fourier transformation from real space to wavenumber leads to $N_z = 50$ points spaced by $\Delta k_z = 2\pi/(N_z a_z)$ within the metamaterial first Brillouin zone, hence to 26 wavenumber values in the interval $k_z \in [0, \pi/a_z]$. Before the Fourier transformation, we multiply a Hann window (*34*) onto the data to suppress possible artifacts from the two sample ends at $n = 1$ and $n = 50$, respectively. In the graphical representations below, we omit the negative wavenumbers due to the symmetry $\omega(k_z) = \omega(-k_z)$. The other end of the beam is closed for the channel-based pressure-wave system and left open for the elastic system, such that in both cases 100% of the wave is reflected at that end. In the presence of finite wave damping, the resulting waves are therefore a mixture of standing waves and propagating waves along the metamaterial-beam axis. At the launching end, the surface termination decides how well the excitation couples to the different modes at a given angular frequency, thus it determines the weight of the mode in the band structures to be shown below. We have optimized the surface terminations of the two three-dimensional structures for roughly equal weights based on numerical finite-element calculations in order to avoid a tedious experimental trial-and-error procedure. In the higher-order-gradient effective-medium description outlined in the previous section, the effect of the surface termination, which is not expected for ordinary acoustical phonons, enters via the fourth- and sixth-order spatial derivatives, which must be matched at an interface in addition to the first and second-order spatial derivative.

Fig. 2 describes and illustrates the microscale samples, and Fig. 3 the macroscale samples. For the manufacturing of the polymer samples shown in Fig. 2, we have used a standard commercial 3D laser nanoprinter (Photonics Professional GT, Nanoscribe) and a commercial photoresist (IP-S, Nanoscribe). Details of the manufacturing process, in which one must cope with a large number of strongly overhanging parts (see Methods for details). To ease the tracking of the transverse and longitudinal components of the displacement vectors, we have added a set of cross-shaped markers (*35*) onto the frame of each unit cell along the z-direction. The markers represent a negligible perturbation with respect to the wave propagation. The macroscopic samples in Fig. 3 have been subdivided into 100 pieces, 2 pieces for each of the $N_z = 50$ unit cells. The individual pieces have been manufactured commercially by 3D printing (fused deposition modeling with PLA). Each unit cell contains a cylindrical hole with a diameter of 9.8 mm in the frame to insert a microphone (Kepo, KPCM-94H65L-40DB-1689). The microphones have been glued into the holes and the 100 pieces have been glued and tightly screwed together to achieve an air-channel system that is sealed with respect to the outside.

Let us briefly give a few more specifics for the two different experiments. For the measurements on the samples in Fig. 2, we excite the samples by a piezoelectric actuator (PL055.31 PICMA®, Physik Instrumente). The samples are imaged from the side by a home-built scanning confocal optical microscope comprising a continuous-wave laser (LCX-532S-200, Oxxius SA) operating at 532 nm wavelength, a microscope objective lens (50X CFI60 TU Plan Epi ELWD, Nikon), and a pinhole in an intermediate imaging plane for moderate z-sectioning (cf. Supplementary Text and Fig. S1). The nanometric transverse and longitudinal components of the displacement vectors of all unit cells at the cross marker positions are obtained by means of optical-image digital cross-correlation analysis (*35*, *36*) on a computer (cf. Supplementary Text and Figs. S2-S3). For the measurements on the sample in Fig. 3, we excite the sample by a loudspeaker (Fane, Sovereign 6-100). We record the local air-pressure modulation by a microphone (Kepo, KPCM-94H65L-40DB-1689) in each of the $N_z = 50$ unit cells. We feed the electrical analog signals into the sound card of a computer, where the data are further processed. For further details, see Methods.

Fig. 4 summarizes resulting exemplary measured raw data for the two experiments and the derived roton band structures within the first Brillouin zone with $|k_z| \leq \pi/a_z$, represented on false-color scales alongside corresponding theoretical calculations for the finite-length ($N_z = 50$) metamaterials beams. In these calculations, damping effects are included phenomenologically (see Materials and Methods). The additional white solid curves are the result of band structure calculations for fictitious lossless metamaterial beams that are infinitely periodic along the z-direction. Here we use Floquet-Bloch periodic boundary conditions along the z-direction and traction-free boundary conditions along the x- and the

y-direction. We use identical geometrical and material parameters as above. For clarity, for the elastic case, we do not depict the twist band in Fig. 4 because the piezoelectric excitation does not couple to it. The gray solid curves are the approximate analytical roton dispersion relations of the higher-order-gradient effective-medium model introduced above.

In Fig. 4, we present two metamaterial experiments that provide evidence for roton dispersion relations under ambient conditions. The experimental data for the ultrasound transverse-like elastic waves (cf. Fig. 2) shown in Fig. 4(a) and for the audible-sound airborne longitudinal pressure waves (cf. Fig. 3) shown in Fig. 4(c) are in good agreement with the respective numerical calculations shown in Fig. 4(b) and (d) performed for the same finite-length metamaterial beams. For the elastic waves, the dispersion relation derived from the longitudinal component of the displacement vectors (cf. Fig. S4) shows an ordinary phonon dispersion relation with larger phase velocity than the transverse branch. In addition, one can see the transverse-like roton because the modes in the metamaterial beam with finite cross section have somewhat mixed transverse/longitudinal character. The finite-length-sample data in Fig. 4 and Fig. S4 agree well with the band structures calculated for infinitely long metamaterials beams (see white solid curves). These band structures are captured qualitatively well by the analytical dispersion relations (see solid gray curves) derived from the approximate higher-order-gradient effective-medium roton model introduced above.

The weight of the peaks in the false-color representation of the measured roton band structures in Fig. 4 should be taken with caution, especially in the frequency region where three peaks versus k_z occur at a given frequency. First, at each frequency, we have normalized the Fourier transforms to unity power density to obtain a unique and unambiguous normalization. As a result, a single peak with fixed shape versus k_z will always have the same weight. Three equally strong peaks versus k_z will have only one third of that weight. By definition, the normalization thereby reduces the peak heights in the roton region. Second, the experimental real-space data additionally comprise noise. This is especially true for the nanometric measurements on the elastic microstructures. The noise contains weight in the spatial Fourier power spectrum and thereby reduces the roton peak heights due to the normalization to equal power density. Third, we recall that the weight of the individual peaks at different k_z can be influenced by the excitation conditions, specifically by the surface termination of the sample at the metamaterial-beam end of the excitation. We have optimized the excitation conditions for roughly equal weight of the peaks. The dependence of the coupling to one of the three modes on the surface termination is a particularity of rotons. In terms of effective-medium descriptions, it is a particularity of the higher-order-gradient generalized wave equation.

Discussion

This particularity of the roton behavior is an opportunity for future work. At a given frequency, at the interface between an ordinary material and a material showing roton-like behavior, for a wave emerging from the ordinary material, one can choose the mode in the roton-like material one wishes to couple to *via* tailoring of the structure at the interface. This means that one can choose between three different wavelengths and behaviors. This aspect brings an entirely new design quality to the interface or transition region.

Finally, our experimental results for transverse elastic waves and longitudinal airborne pressure waves in metamaterials can likely also be transferred to other areas of physics, for example to electromagnetism and optics.

Materials and Methods

Band structure calculations

For the elastic and air-borne sound roton metamaterials, respectively, we numerically find the angular eigenfrequency $\omega_i(\vec{k})$ for the band with band index i at wave vector $\vec{k}$ from the eigenvalue equation derived from linear elasticity theory

$$\frac{E}{2(1+\nu)(1-2\nu)}\vec{\nabla}\left(\vec{\nabla}\cdot\vec{u}_{\vec{k},i}(\vec{r})\right)+\frac{E}{2(1+\nu)}\vec{\nabla}^2\vec{u}_{\vec{k},i}(\vec{r})=-\rho\omega_i^2(\vec{k})\vec{u}_{\vec{k},i}(\vec{r}), \tag{S1}$$

and acoustic theory

$$\frac{E}{2(1+\nu)(1-2\nu)}\vec{\nabla}\cdot\left(\vec{\nabla}\tilde{P}_{\vec{k},i}(\vec{r})\right)=-\frac{\omega_i^2(\vec{k})}{v_{\mathrm{air}}^2}\tilde{P}_{\vec{k},i}(\vec{r}), \tag{S2}$$

respectively. Here, $\vec{u}_{\vec{k},i}(\vec{r})$ and $\tilde{P}_{\vec{k},i}(\vec{r})$ represent the displacement eigenmode and pressure eigenmode for the two metamaterials, respectively. We solve these equations by using the Solid Mechanics Module and the Pressure Acoustic Module, respectively, in the commercial software Comsol Multiphysics, specifically using its MUMPS solver. Floquet-Bloch periodic boundary conditions are applied along the z direction, $\vec{k}=k_z\mathbf{e}_z$, of the metamaterial sample containing $N_x\times N_y=2\times 2$ and $N_x\times N_y=1\times 1$ unit cells, respectively, in its cross section. Traction-free boundary conditions are applied to all interfaces to voids (air or vacuum) for the elastic roton metamaterial. Sound rigid boundary conditions are applied to all interfaces to solids for the air-borne sound case. We choose $E=4.19$ GPa for the Young's modulus, $\nu=0.4$ for the Poisson's ratio, and $\rho=1140\ \mathrm{kg/m^3}$ for the mass density of the constituent material of the elastic metamaterial. We choose a speed of sound in air of $v_{\mathrm{air}}=340\ \mathrm{m/s}$ for the air-borne sound metamaterial.

Finite-size sample calculations

The responses of the finite-size elastic roton metamaterial and the air-borne sound roton metamaterial samples are calculated in the frequency domain by using the equations

$$\frac{E}{2(1+\nu)(1-2\nu)}\vec{\nabla}\left(\vec{\nabla}\cdot\vec{u}(\omega,\vec{r})\right)+\frac{E}{2(1+\nu)}\vec{\nabla}^2\vec{u}(\omega,\vec{r})=-\rho\omega^2\vec{u}(\omega,\vec{r}), \tag{S3}$$

and

$$\vec{\nabla}\cdot\left(\vec{\nabla}\tilde{P}(\omega,\vec{r})\right)=-\frac{\omega^2(\vec{k})}{v_{\mathrm{air}}^2}\tilde{P}(\omega,\vec{r}), \tag{S4}$$

with $\vec{u}(\omega,\vec{r})$ and $\tilde{P}(\omega,\vec{r})$ representing the displacement and the pressure modulation responses at angular frequency ω, respectively. The equations are solved by using the Solid Mechanics Module and the Pressure Acoustic Module in the commercial software Comsol Multiphysics, again with its MUMPS solver. We apply a transverse displacement field, $\vec{u}(\omega,\vec{r}=0)=(u_0,0,0)\cos(\omega t)$, and a pressure-modulation field, $\tilde{P}(\omega,\vec{r}=0)=$

$P_0\cos(\omega t)$, to the bottom end of the two samples, respectively, to model time-harmonic excitation in the experiment. At the other boundaries of the samples, traction-free boundary conditions and acoustic rigid boundary conditions are applied, respectively. The material parameters are the same as in Band structure calculations except that an imaginary part of the Young's modulus E and of the sound velocity v_{air}, respectively, are used to mimic damping effects that occur in the experiments. The imaginary part is set to 5% of the real part of the Young's modulus E and 2% of the real part of the sound velocity v_{air}, respectively.

Sample fabrication of the elastic roton metamaterial

We fabricate the microscale metamaterials using 3D laser microprinting (Professional GT, Nanoscribe GmbH). We use a $25\times$ objective lens (numerical aperture $= 0.8$, Carl Zeiss), which is dipped directly into the liquid photoresist (IP-S, Nanoscribe GmbH). The laser focus is scanned using two galvanometric mirrors at a focus speed of $0.125\ \mathrm{m/s}$. The mean laser power is set to $27.5\ \mathrm{mW}$, measured at the entrance pupil of the microscope lens.
The underlying 3D models are created using the commercial software package COMSOL Multiphysics (COMSOL Inc.). Subsequently, these are transcribed into machine code using the software Describe (Nanoscribe GmbH). We choose a hatching distance of $300\ \mathrm{nm}$, a slicing distance of $700\ \mathrm{nm}$, and a stitching distance of $200\ \mu\mathrm{m}$.
Since pending and overhanging structures cannot be fabricated easily, the unit cell is spilt into several parts that are printed consecutively. To ensure a single connected sample during the whole printing process, the writing direction is switched multiple times between $+z$ and $-z$. Furthermore, we add support structures and scaffoldings, which become part of the structure in a later printing step and therefore do not need to be removed. More details can be found in the original GWL-files that are published in [Enter repository].
Furthermore, a bottom plate is added to facilitate handling of the samples and to ensure proper contact to the piezoelectric element when being glued. This bottom plate is printed using a focus speed of $0.140\ \mathrm{m/s}$, a laser power of $50\ \mathrm{mW}$, a hatching distance of $0.5\ \mu\mathrm{m}$, and a slicing distance of $1.5\ \mu\mathrm{m}$.
After exposure, the excess photoresist is removed in a beaker of MR-Dev 500 and acetone for 20 minutes each, followed by critical-point drying (Leica EM CPD300, using CO_2).

Elastic experiment setup

The elastic metamaterial sample is glued onto the side of an aluminum cuboid, which is fixed to a piezoelectric actuator such that the main axis of the actuator lies in the transverse plane of the metamaterial sample. Since the metamaterial sample exceeds the optical field of view of the confocal optical microscope setup, the actuator is mounted on an xyz-translation stage using piezo-inertia drives for sample manipulation. This assembly is positioned in the focal plane of the microscope objective lens (cf. Fig. S1) to enable a side view of the metamaterial sample. The back-reflected light is measured with an avalanche photodiode module that outputs a photovoltage proportional to the incident light power.

Elastic single-frequency excitation measurement

The metamaterial sample is excited by driving the piezoelectric actuator with an amplified sinusoidal voltage. The data acquisition unit of the confocal optical microscope is synchronized to this excitation signal. This synchronization is crucial for image generation and for subsequently obtaining the phase information of the displacement trajectory at each sample position. Data acquisition consists of scanning a spatial region of interest (ROI) on the excited sample. The ROI size is chosen to span 60×60 pixels over a rectangular sample area of $30 \times 30\ \mu\mathrm{m}^2$. At each pixel, a time series of the photovoltage is acquired before the next pixel is measured. A total of 51 ROIs are investigated for each sample. The zeroth ROI is located on the base plate of the sample providing quantitative information about phase and amplitude of the sample excitation. The remaining 50 ROIs are placed on the cross-shaped markers on the outer frame of each metamaterial layer. The frequency resolution of the excitation is set to $\Delta f = 5$ kHz. The excitation frequency is kept constant until all ROIs have been measured for that frequency. Between switching of the excitation frequency and starting a new time series, the data acquisition is halted for about 200 ms. This waiting time acts as a buffer for the sample to respond to the new excitation signal. Images for the digital-image cross-correlation analysis are generated by combining the set of time series for each frequency at every ROI respectively, utilizing the synchronization between the excitation signal and the data acquisition (cf. Fig. S2).

Acoustic experiment setup

Each unit cell of one acoustic metamaterial sample is divided into two identical parts, thanks to the symmetry with respect to the horizontal plane parallel to the xy-plane. A set of 100 identical pieces is fabricated by 3D printing (3DHubs). The two parts forming each of the 50 unit cells are joined together with the help of screws and an acrylic plastic filler (Mastic, Axton) to ensure sealing with respect to air. In each unit cell, a microphone is positioned inside a hole on the side of a half unit cell. The hole in the other half is closed with hot glue. A loudspeaker (diameter 165 mm) is fixed to an extra unit cell printed with a circular face (cf. Fig. S5). The extra unit cell is added at the entrance of the metamaterial sample in order to couple sound into the channel-based metamaterial sample. The other end of the metamaterial beam is terminated by a metal plate in order to obtain boundary conditions comparable to the elastic case. The entire metamaterial structure is compressed by threaded rods to ensure mechanical stability (cf. Fig. S6).

Acoustic single-frequency excitation measurement

A sinusoidal signal at a given frequency is produced by a computer, subsequently amplified, and send to the loudspeaker. Using the sound card of the computer, the signals received by two microphones are recorded simultaneously, at the Nth unit cell and at the entrance unit cell where the excitation is fed into. The latter signal is used as a reference for phase and amplitude measurements. The sinusoidal signal duration is set to 1 s, resulting in a 1 Hz frequency resolution. The measurement is performed for all frequencies of interest and for the $N_z = 50$ units cells, including a 1 s silence between each recording to ensure that a silent steady-state is recovered. To further validate the single-frequency excitation measurements, additional experiments with white-noise excitation have also been performed. The obtained first band agrees well with that obtained by single-frequency excitation and the higher bands agree well with corresponding theoretical calculations (cf. Fig. S6 and Fig. S7).

References

1. Landau, L. Theory of the Superfluidity of Helium II. *Phys. Rev.* **60**, 356 (1941).
2. Feynman, R. P. Atomic theory of the two-fluid model of liquid helium. *Phys. Rev.* **94**, 262 (1954).

3. Feynman, R. P. Atomic theory of liquid helium near absolute zero. *Phys. Rev.* **91**, 1301 (1953).
4. Henshaw, D. G. & Woods A. D. B. Modes of atomic motions in liquid helium by inelastic scattering of neutrons. *Phys. Rev. Lett.* **121**, 1266 (1961).
5. Griffin, A. & Allan G. *Excitations in a Bose-condensed liquid* (Cambridge University Press, 1993).
6. Bogoliubov, N. On the theory of superfluidity. *J. Phys.* **11**, 23 (1947).
7. Feynman, R. P. & Cohen M. Energy spectrum of the excitations in liquid helium. *Phys. Rev.* **102**, 1189 (1956).
8. Schneider, T. & Enz C. P. Theory of the Superfluid-Solid Transition of ^{4}He. *Phys. Rev. Lett.* **27**, 1186 (1971).
9. Glyde, H. R. & Griffin A. Zero sound and atomiclike excitations: The nature of phonons and rotons in liquid ^{4}He. *Phys. Rev. Lett.* **65**, 1454 (1990).
10. Kalman, G. J., Hartmann P., Golden K. I., Filinov A. & Donkó Z. Correlational origin of the roton minimum. *Europhys. Lett.* **90**, 55002 (2010).
11. Woods, A. D. B. Neutron inelastic scattering from liquid helium at small momentum transfers. *Phys. Rev. Lett.* **14**, 355 (1965).
12. Beauvois, K., et al. Microscopic dynamics of superfluid ^{4}He: A comprehensive study by inelastic neutron scattering. *Phys. Rev. B* **97**, 184520 (2018).
13. Maris, H. J. Phonon-phonon interactions in liquid helium. *Rev. Mod. Phys.* **49**, 341 (1977).
14. Godfrin, H., et al. Dispersion relation of Landau elementary excitations and thermodynamic properties of superfluid He 4. *Phys. Rev. B* **103**, 104516 (2021).
15. Godfrin, H., et al. Observation of a roton collective mode in a two-dimensional Fermi liquid. *Nature* **483**, 576-579 (2012).
16. Koehler, T. R., & Werthamer, N. R. Computation of phonon spectral functions and ground-state energy of solid Helium. I. bcc phase. *Phys. Rev. A* **5**, 2230 (1972).
17. Girvin, S. M., MacDonald A. H. & Platzman P. M. Magneto-roton theory of collective excitations in the fractional quantum Hall effect. *Phys. Rev. B* **33**, 2481 (1986).
18. Kukushkin, I. V., Smet J. H., Scarola V. W., Umansky V. & von Klitzing K. Dispersion of the excitations of fractional quantum Hall states. *Science* **324**, 1044-1047 (2009).
19. Kukushkin, I. V., Umansky V., von Klitzing K. & Smet J. H. Collective modes and the periodicity of quantum Hall stripes. *Phys. Rev. Lett.* **106**, 206804 (2011).
20. Henkel, N., Nath R. & Pohl T. Three-dimensional roton excitations and supersolid formation in Rydberg-excited Bose-Einstein condensates. *Phys. Rev. Lett.* **104**, 195302 (2010).
21. Lahrz, M., Lemeshko M. & Mathey L. Exotic roton excitations in quadrupolar Bose-Einstein condensates. *New J. Phys.* **17**, 45005 (2015).
22. Ha, L., Clark L. W., Parker C. V., Anderson B. M. & Chin C. Roton-Maxon Excitation Spectrum of Bose Condensates in a Shaken Optical Lattice. *Phys. Rev. Lett.* **114**, 55301 (2015).
23. Chomaz, L., et al. Observation of roton mode population in a dipolar quantum gas. *Nat. Phys.* **14**, 442-446 (2018).
24. Petter, D., et al. Probing the Roton Excitation Spectrum of a Stable Dipolar Bose Gas. *Phys. Rev. Lett.* **122**, 183401 (2019).
25. Schmidt, J. N., et al. Roton Excitations in an Oblate Dipolar Quantum Gas. *Phys. Rev. Lett.* **126**, 193002 (2021).
26. Kishine, J., Ovchinnikov A. S. & Tereshchenko A. A. Chirality-Induced Phonon Dispersion in a Noncentrosymmetric Micropolar Crystal. *Phys. Rev. Lett.* **125**, 245302 (2020).

27. Chen, Y., Kadic M. & Wegener M. Roton-like acoustical dispersion relations in 3D metamaterials. *Nat. Commun.* **12**, 3278 (2021).
28. Fleury, R. Non-local oddities. *Nat. Phys.*, (2021).
29. Cummer, S. A., Christensen J. & Alù A. Controlling sound with acoustic metamaterials. *Nat. Rev. Mater.* **1**, 16001 (2016).
30. Bertoldi, K., Vitelli V., Christensen J. & Van Hecke M. Flexible mechanical metamaterials. *Nature Reviews Materials* **2**, 1 (2017).
31. Eringen, A. C. Linear theory of micropolar elasticity. *J. Math. Mech.* **15**, 909 (1966).
32. Eringen, A. C. *Microcontinuum field theories* (Springer, 1999).
33. Chen, Y., Frenzel T., Guenneau S., Kadic M. & Wegener M. Mapping acoustical activity in 3D chiral mechanical metamaterials onto micropolar continuum elasticity. *J. Mech. Phys. Solids* **137**, 103877 (2020).
34. Smith III, J. O. *Spectral audio signal processing* (W3K publishing, 2011).
35. Frenzel, T., Köpfler J., Naber A. & Wegener M. Atomic scale displacements detected by optical image cross-correlation analysis and 3D printed marker arrays. *Sci. Rep.* **11**, 2304 (2021).
36. Pan, B., Qian K., Xie H. & Asundi A. Two-dimensional digital image correlation for in-plane displacement and strain measurement: a review. *Meas. Sci. Technol.* **20**, 62001 (2009).
37. Jordan, C. & Jordán K. *Calculus of finite differences* (American Mathematical Soc., 1965).
38. Shannon, C. E. Communication in the presence of noise. *Proceedings of the IRE* **37**, 10-21 (1949).
39. Frenzel, T., Köpfler J., Jung E., Kadic M. & Wegener M. Ultrasound experiments on acoustical activity in chiral mechanical metamaterials. *Nat. Commun.* **10**, (2019).
40. Negrean, A. & Mansvelder H. D. Optimal lens design and use in laser-scanning microscopy. *Biomed. Opt. Express* **5**, 1588-1609 (2014).
41. Welch, P. The use of fast Fourier transform for the estimation of power spectra: a method based on time averaging over short, modified periodograms. *IEEE Transactions on audio and electroacoustics* **15**, 70-73 (1967).

Acknowledgments

We thank Jonas Wohlgemuth (KIT) and Gwenn Ulliac (FEMTO-ST) for providing preliminary macroscopic 3D printed samples, Jannis Weinacker (KIT) for help in the construction of the measurement setup at KIT, Sebastian Kalt for help in taking the 3D fluorescent images of the microscopic samples, and Martin Bastmeyer (KIT) for letting us use this confocal laser scanning fluorescence microscope.

Funding:

The Alexander von Humboldt Foundation (YC)

The Deutsche Forschungsgemeinschaft (DFG, German Research Foundation) under Germany's Excellence Strategy via the Excellence Cluster “3D Matter Made to Order” (EXC-2082/1-390761711), which has also been supported by the Carl Zeiss Foundation through the “Carl-Zeiss-Foundation-Focus@HEiKA”, by the State of Baden-Württemberg, and by the Karlsruhe Institute of Technology (MW)

the Helmholtz program “Materials Systems Engineering” (MW)

EIPHI Graduate School ANR-17-EURE-0002 (MK)

Author contributions:

J.A.I.M. performed the experiments at Besancon, M.F.G. the experiments at KIT. T.F. manufactured the samples at KIT. Y.C. and M.K. designed both experiments. Y.C. performed all numerical calculations. M.W. wrote the first draft of the paper. V.L. and M.W. supervised the overall effort. All authors contributed to the interpretation of the results and to the writing of the manuscript.

Competing interests: Authors declare that they have no competing interests.

Data and materials availability: The data that support the plots within this paper and other findings of this study are available from the corresponding author upon reasonable request and are published on the open access data repository of the Karlsruhe Institute of Technology [Enter repository].

Figures and Tables

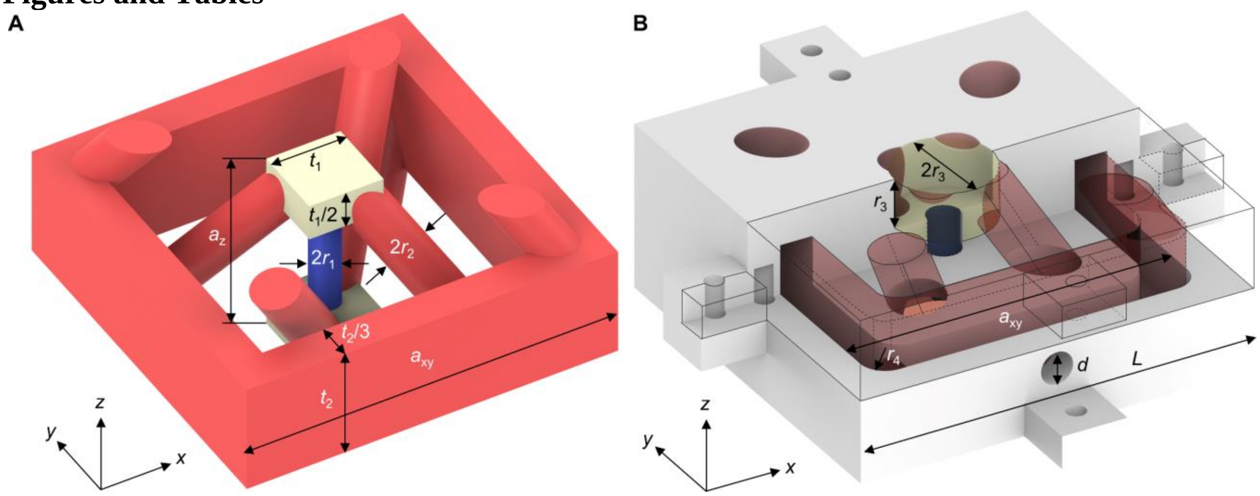

Fig. 1. Two blueprints for roton metamaterials. (**A**) Three-dimensional microstructure unit cell of a metamaterial beam (*26*) supporting transverse-like rotons for elastic-wave propagation along the z-direction. The blue and red cylinders are responsible for the nearest-neighbor interactions and third-nearest-neighbor interactions, respectively, between the yellow masses. Different colors are for illustration only; the entire structure is made from a single polymer material. The geometrical parameters are indicated. (**B**) Unit cell of the channel-based metamaterial beam supporting rotons for airborne longitudinal pressure waves along the z-direction in the channel system. This unit cell is roughly complementary to the unit cell in (**A**), and is composed of a bottom piece and an upper piece, whose front half is intentionally removed to show the inner compartment (yellow). The cylindrical channels for air pressure propagation are rendered semi-transparent in red and blue, respectively, in analogy to (**A**). Here, the masses in (**A**) correspond to cylindrical compartments. A microphone is installed in the through-hole with diameter d on the front wall of the lower piece. The other holes are for alignment and assembly. Only geometrical parameters different from those in (**A**) are given in (**B**).

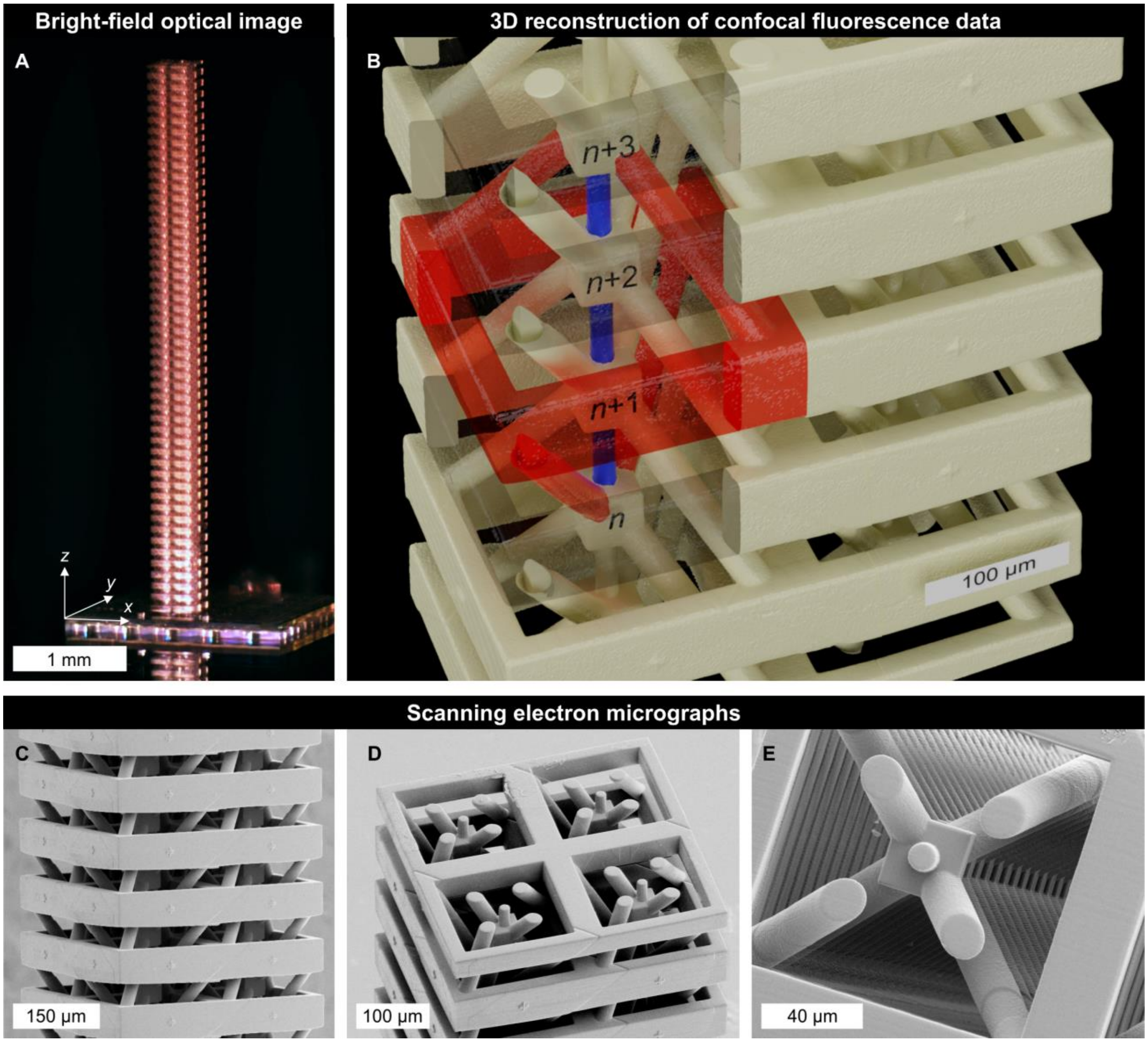

Fig. 2. Roton metamaterial microstructures for elastic waves. The shown polymer samples, which have been manufactured in one piece by multiphoton 3D laser microprinting, follow the blueprint shown in Fig. 1(**A**). (**A**) overview of a sample imaged with a wide-field microscope. (**B**) 3D iso-intensity surface acquired with a confocal fluorescence optical microscope (LSM 800, Zeiss) utilizing the autofluorescence of the polymer. Scale bar and labels added in postprocessing using blender™. Parts of the unit cell frames are made to appear transparent to reveal the interior. The third-nearest-neighbor coupling is colored in red, the nearest-neighbor coupling in blue. (**C**)-(**E**) Scanning electron micrographs of (**C**) the unit cell frames, (**D**) the uppermost layers, and (**E**) a view along the center axis of one column of unit cells.

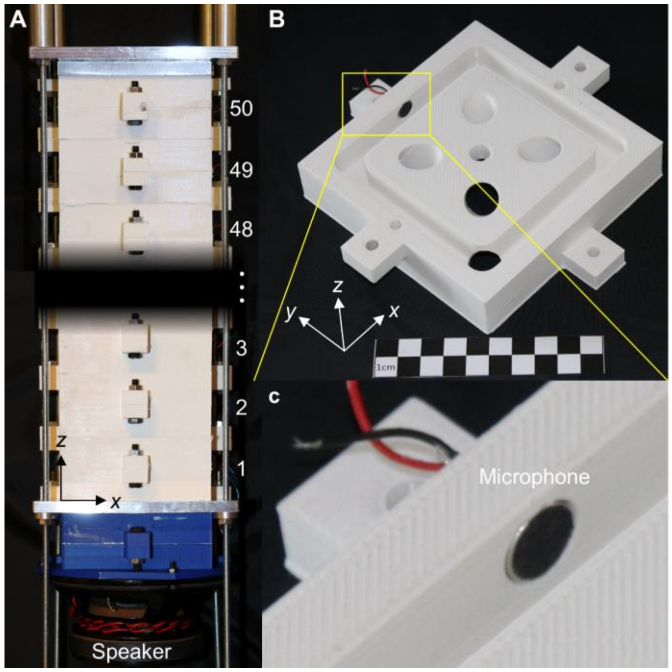

Fig. 3. Roton metamaterial sample for airborne sound. (**A**) The 3D printed polymer sample follows the blueprint shown in Fig. 1(**B**). It has been assembled from 100 individual pieces, 2 for each of the $N_z = 50$ unit cells. The metamaterial sample has a length of 2 m along the z-direction. Therefore, only the bottom part and the top part are shown here. (**B**) One of the two pieces for one unit cell. (**C**) Zoom-in view of the highlighted rectangle region in (**B**) showing an installed microphone on the side wall.

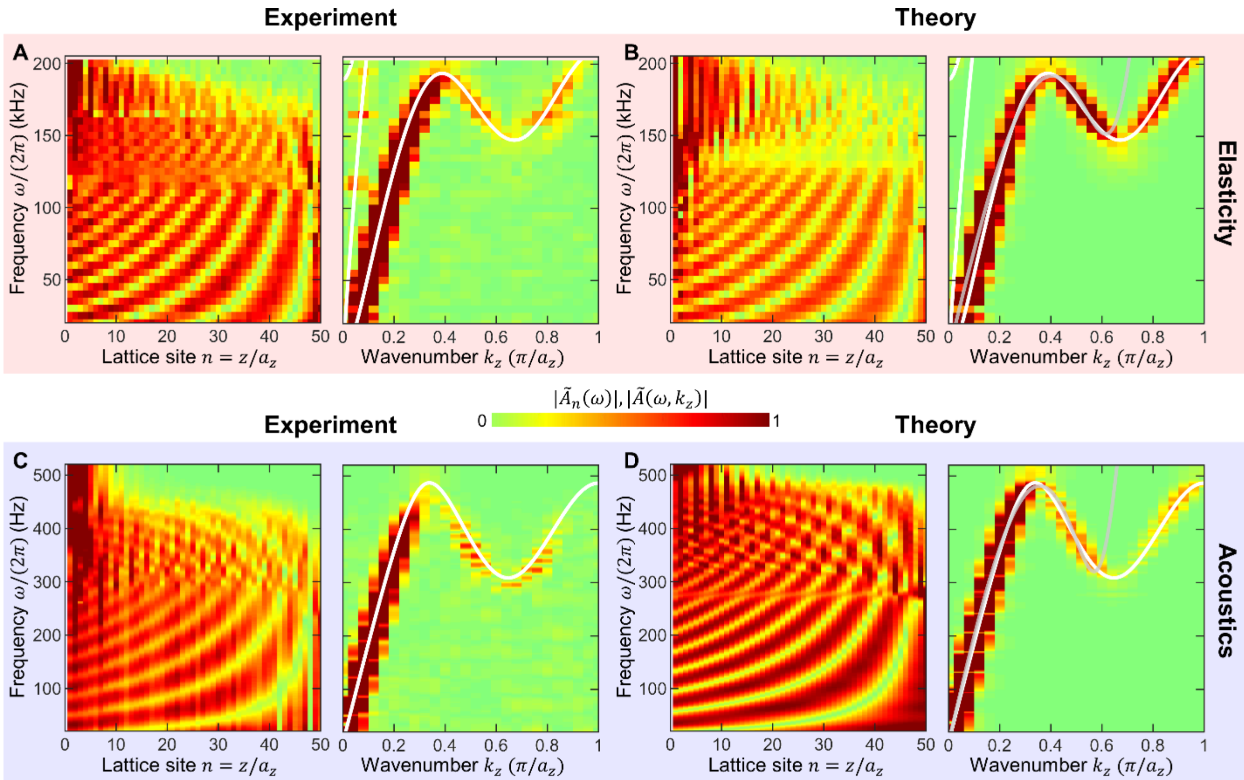

Fig. 4. Measured and calculated roton dispersions. (**A**) Measured raw data (left) for the sample in Fig. 2 versus position and frequency and derived roton band structure (right). (**B**) Corresponding numerically calculated behavior for the same finite sample length and including damping. (**C**) as (**A**), but for the sample in Fig. 3. (**D**) Numerically calculated behavior corresponding to the measurements in (**C**). The white solid curves are the calculated roton band structures for a lossless metamaterial beam that is infinitely extended along the z-direction. For the elastic metamaterial, we use the geometrical parameters: $a_{xy} = 200$ µm, $a_z = 100$ µm, $2r_1 = 16.8$ µm, $2r_2 = 25.2$ µm, and $t_2 = 60$ µm. For the airborne metamaterial, we use the geometrical parameters: $a_{xy} = 100$ mm, $a_z = 50$ mm, $2r_1 = 10$ mm, $2r_2 = 16$ mm, $2r_3 = 30$ mm, $t_2 = 30$ mm, $d = 9.8$ mm, $r_4 = 7.5$ mm, and $L = 120$ mm. The gray curves in panels (**B**) and (**D**) correspond to the approximate analytical dispersion relations of the higher-order-gradient effective-medium model with parameters c_2, c_4, and c_6 fitted to the interval $k_z \in [0, 0.6 \times \pi/a_z]$.

Supplementary Materials

Supplementary Text
Figs. S1 to S7
Table S1
References (*37–41*)